Symphotic Multiplexing Medium at Microwave Frequencies

Divya Pande,* Jonah Gollub, Roberto Zecca, Daniel L. Marks, and David R. Smith
Department of Electrical and Computer Engineering, Duke University, Durham, North Carolina 27708, USA

(Received 10 December 2019; revised manuscript received 14 January 2020; accepted 16 January 2020; published 13 February 2020)

As opposed to metasurfaces, which can produce a single output waveform in response to a single input waveform, volumetric metamaterials have the ability to perform independent functions on many distinct input waveforms. Here, we present an experimental demonstration of this multiplexing capability using a volumetric metamaterial designed using the symphotic method, which realizes highly efficient multiplexing structures in the strong scattering limit. In contrast to perturbative design methods such as volume holography that are only applicable in weakly scattering media, we provide a comprehensive approach that takes into consideration design and fabrication constraints and that can be verified in simulations. We then demonstrate an experimental realization of a symphotic device operating at a frequency of 10 GHz, which has been optimized for three distinct input waveforms corresponding to three distinct output waveforms. The device is realized using a low-loss three-dimensionally printed material. The symphotic device consists of a lattice of dielectric cylindrical elements with varying radii, excited in a parallel-plate waveguide to enforce two-dimensional field symmetry. The experimental results show excellent agreement with analytical coupled-dipole-method simulations and finite-element simulations. The experiments further demonstrate the scalability of symphotic metamaterials and their viability for advanced rf and optical devices.

DOI: 10.1103/PhysRevApplied.13.024033

I. INTRODUCTION

An important class of optical devices consists of those that convert an input waveform into an arbitrary output waveform. While there are many approaches to the design of such devices, a particularly intuitive method is that of holography, in which the desired output waveform, or *object wave*, is propagated back to an aperture plane and interfered with the incident wave form, or *reference wave*, producing a phase-and-amplitude variation over the plane, or *hologram*. When this spatially varying phase-and-amplitude distribution is added to the reference wave, the desired object wave is produced. Surface holography is a conceptually straightforward, yet powerful, design methodology that enables arbitrary control over wave fronts as long as the required amplitude and phase variations can be achieved in some physical medium.

If only the properties of a surface can be modified, then at most one function (at a given wavelength) can be designed into a surface hologram. Once the interference pattern between the back-propagated object and reference waves has been determined, all of the available degrees of freedom are exhausted; any other spatially distinct incident wave at the same wavelength will produce a different spatial pattern at the aperture plane. The subsequent scattering is thus uncontrolled, since the hologram has been designed specifically for one particular spatial pattern.

To construct a device that supports multiple functions, such as is illustrated in Fig. 1, the properties of a medium occupying a finite volume must be subject to variation. Holography can also serve as the design approach in this context but now an interference pattern between the object and reference waves over some volume of space must be realized, or a *volume hologram*. The advantage of a volume hologram is that many distinct reference waves can be incorporated into the volume hologram, each producing a distinct object wave, such that the volume hologram can be considered a multiplexing device. For this reason, volume holograms have been considered for many applications that require massive multiplexing capabilities, including optical computing, spectral imaging, data storage, and multispectral sensing.

While volume holography might seem the ideal design approach for multiplexing optics and has been used in several demonstrations [1–8], the concept is only valid in the weakly scattering limit, where the reference wave is left unperturbed as it travels through the volume hologram. In reality, if there is any appreciable conversion of the reference wave to the object wave—as would be necessary for efficient devices—the reference wave will be altered as it transits the volume and the holographically designed medium properties are no longer applicable. So, while

*dp197@duke.edu

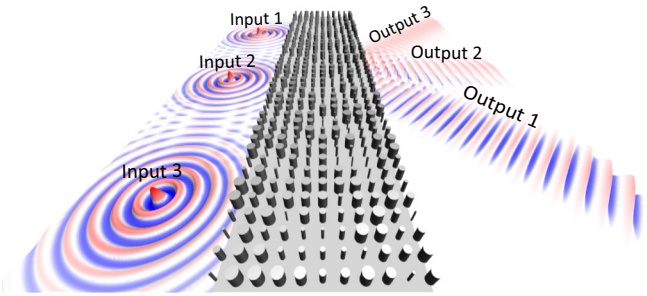

FIG. 1. An illustration of a symphotic device that transforms three spatially distinct input sources to three distinct Gaussian beam output waveforms.

volume holography is conceptually attractive due to its design simplicity, it cannot lead to efficient optical devices.

In general, an inverse problem must be solved to find the properties of a medium capable of converting an arbitrary set of input fields incident on its boundary to a set of desired output fields. If high-efficiency multiplexing in particular is to be achieved, stronger scattering responses must be included and leveraged. One design approach introduced by Vučković *et al.* [9–15] can generate high-efficiency multiplexing devices by optimizing the topology of a mixture of naturally occurring materials in a volume. Similar approaches have been explored by Yablonovitch *et al.* [16–18]. This family of strategies is effective but computationally intensive and limited to fairly small volumes and numbers of functions. To encode a large number of functions in the same device, the volume considered must be large enough to afford it the necessary degrees of freedom to implement all the desired operations.

The recently published *symphotic* design method [19] is an effective means of attacking the inverse design problem. It yields designs for devices that are able to multiplex many functions with high efficiency and low crosstalk, even when encoded at the same frequency and polarization. This emphasis on multiplexing has led to the term "symphotic," which indicates a medium that can perform a large number of simultaneous optical functions with high efficiency. In principle, it is possible to use the symphotic method to design devices that operate at any frequency in the electromagnetic spectrum, up to the visible and ultraviolet range. The underlying assumption to the method is that a medium can be constructed out of very small scattering elements, such that each element may be accurately described as an electromagnetic point dipole. This assumption, known as the *discrete-dipole approximation*—originally used in the field of astronomy to model interstellar grains [20–24]—requires all elements to be of subwavelength dimension and to interact solely through their dipolar fields. The dipole assumption has more recently found extensive application in the modeling of artificial media, such as metamaterials [25–33], metasurfaces, plasmonic systems [34–37], and, most recently, symphotic devices [19,38]. In this context, it is more appropriate to refer to the dipole framework as the coupled-dipole model (CDM), since once elements are found that scatter as dipoles, all interactions among the dipoles are rigorously taken into account. By reducing a medium to a set of dipole-like elements, the requisite forward model can be efficiently solved (the CDM scales in operation as $N \log N$, where N is the number of point dipoles [22]). Since the inverse design of a symphotic medium requires many iterative solutions of the scattering problem, reduction of the number of unknowns via the dipole description enables extremely large systems to be designed, with potentially thousands of simultaneous functions encoded. More recently, Fan *et al.* have published a formulation akin to the symphotic method [39,40].

In this work, we present an experimental demonstration of a symphotic medium designed to convert the fields from three line sources at different locations to three outgoing beams, as illustrated in Fig. 1. The fabricated symphotic medium consists of a regular grid of all-dielectric elements, to keep losses low. Other choices, such as metallic and/or resonant scatterers, have inherently larger ohmic losses and would be more challenging to incorporate into an efficient design. For ease of fabrication and testing, we choose the microwave X band (8–12 GHz) for the experiments and fabricate the symphotic devices using a three-dimensionally (3D) printed low-loss polymer, polylactic acid (PLA). For this demonstration, we limit the design and testing to a two-dimensional (2D) structure, invariant along the out-of-plane axis and with a uniform electric field polarized along the cylinder axes. This work is structured as follows: in Sec. II, we briefly summarize the symphotic method. Since the electromagnetic properties of 3D-printed materials may vary significantly as a function of the printing-path algorithms, the extrusion properties of the material, and the infill density, we characterize several polymers in order to select the most appropriate one for our application. The results are presented in Sec. III. Next, we introduce the cylindrical scatterers that we use to realize the symphotic design. To convert the symphotic design, which is expressed in terms of dipole polarizabilities, into a geometric design, we find the relationship between the cylinder radius and the polarizability, using both theory and simulation, in Sec. IV. We check our assumption that the cylinders scatter like point dipoles in Sec. V, again using both theory and simulation. This process also suggests an upper limit on the cylinder radii and a choice of lattice parameter. The device fabrication is discussed in Sec. VI. We design and fabricate two devices: a simplex (one-function) device that collimates a line source into a beam and a multiplex (multifunction) device that converts three different line sources into three separate beams, independently, efficiently, and with minimal crosstalk. In Sec. VII, we introduce our experimental

apparatus, a field-mapping parallel-plate waveguide, and present the behavior of the designed devices, comparing measured fields with predictions from the symphotic or CDM modeling and full-wave simulations. We draw conclusions and outline future directions in Sec. VIII.

II. THE SYMPHOTIC METHOD

The task of finding a scattering medium given the specification of pairs of input-output waves is a form of the inverse-scattering problem. This inverse problem has unfavorable properties, such as nonlinearity, poor conditioning, numerical instability, and no guarantees of uniqueness or existence of solutions. There are many simplified and tractable models, such as the first Born approximation [41], which linearize the problem and make it easier to solve but are only applicable to weakly scattering media. Media that scatter more strongly are a necessity if one wants to design highly efficient multifunctional electromagnetic devices. The symphotic design methodology, originally introduced in Refs. [19,42], provides a mechanism for designing such media. We now give a brief summary of this design methodology, which does not simplify the problem by linearizing it and is thus more general.

The symphotic method provides a way to design such media, by combining (1) the coupled-dipole model (CDM) [20,21,23,24,29], (2) the variational principle [43], and (3) an adjoint-state approach to separate the inverse-scattering problem into two more easily solved direct-scattering subproblems. The reader is encouraged to refer to Refs. [19,38,42] for more background and details.

In brief, solutions to the design problem can be found at the stationary points of a functional F, which depends linearly on the electric fields of both direct-scattering subproblems and on the scattering properties of the medium. In our case, the scattering behavior is represented by the electric polarizabilities of nondispersive dielectric elements acting as point "dipoles," α, which acquire an electric dipole moment $p = \alpha E$, where E is the total electric field, inclusive of the dipole fields, at the dipole location. The subproblem fields are denoted as E and E^a and at the solution points they relate as $E^* = E^a$ [19,38,42]. For N_w pairs of input-output waves, the gradient of the functional F with respect to polarizabilities α is

$$\nabla_\alpha F = -\sum_{n=1}^{N_w} w_n E_n^{a*} \circ E_n, \tag{1}$$

where w_n are optional weighting factors and $\circ$ is the element-wise product. We use the $e^{j\omega t}$ convention for time phasors. The symphotic method starts from the specification of input-output pairs and a hypothesis of an initial medium (its values of α) and alternates field-solving steps using the CDM and updates to the polarizabilities, using $\nabla_\alpha F$ in a simple gradient-descent method:

$$\alpha^{(p+1)} = \alpha^{(p)} - \gamma\,(\nabla_\alpha F)^{(p)}, \tag{2}$$

where γ is a small step-size parameter. The iteration may include Lagrange multipliers to constrain the values of α within a set interval, which is typically determined by the physical limitations on the realized scattering element, as discussed in Sec. V. The "design optimality" of each input-output transformation may be calculated as [19,38]

$$\eta_n \equiv \left| \frac{\langle E_n^a, E_n \rangle}{\sqrt{\langle E_n, E_n \rangle \langle E_n^a, E_n^a \rangle}} \right|^2, \tag{3}$$

using the conjugated inner product $\langle x, y \rangle \equiv x^\dagger y$. This "design optimality" represents the degree to which the design approaches the limit of what is achievable given the device volume. In other words, it quantifies how well the portion of the input wave that reaches the device boundary is transformed into the desired output wave.

III. MATERIAL CHARACTERIZATION

To ensure accurate device design, it is necessary to precisely characterize the electromagnetic properties of the dielectric material composing the scatterers. Since our devices are fabricated by additive manufacturing techniques, it is not enough to know the electromagnetic properties of the extrusion filament material. We must measure the properties of the material, postextrusion, to account for variations in infill density and layer thickness.

Material characterization is performed via measurements of the printed material within a waveguide. The experimental setup consists of an Agilent N5222A vector-network analyzer (VNA), semirigid cables extending from the test ports to WR-90 waveguide adapters, and a 10-mm-long waveguide section filled with the material to be characterized. The geometry of the waveguide has standard WR-90 dimensions of $a = 22.86$ mm and $b = 10.16$ mm, as shown in Fig. 2, such that only a TE_{10} mode propagates for the given frequency range. Scattering (S) parameters are measured across the network using the VNA. To extract the electromagnetic properties, the measurement plane of the scattering parameters must be established at the front and back of the material sample, and error, due to other scattering imperfections (connectors, cable loss, impedance mismatch, etc.) eliminated. A thru, reflect, line (TRL) calibration method is used for this purpose. This approach is more accurate than other methods [44–46]; it is very repeatable and requires measurements of only three simple standards [thru, reflect (short), and a line]. Since the X-band upper-to-lower frequency ratio is less than 8:1, we need only one line standard to characterize the frequency band we are interested in [47]. We choose the midfrequency, i.e., 10 GHz, to calculate its length. The

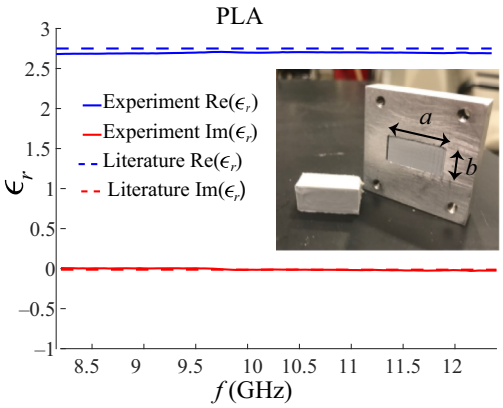

FIG. 2. Experimental and literature values for the real and imaginary parts of the relative permittivity of 3D-printed gray PLA (100% fill fraction). The experimental values are determined using the waveguide-extraction method. The inset shows a PLA sample inside the X-band rectangular waveguide. Its dimensions are $a = 22.86$ mm and $b = 10.16$ mm.

phase length of a line standard can be between 20 and 160 electrical degrees with respect to the thru standard [47]. We fabricate a 10-mm-long line standard with a 90° phase shift at 10 GHz; this results in good calibration across the entire X band. Once the calibration is performed, we measure all four S parameters of the waveguide containing the 3D-printed samples. We use the Nicolson-Ross-Weir (NRW) algorithm to extract the complex permittivity from the S parameters [48,49]. Here, we assume the complex permeability value of the 3D-printed samples to be $\mu_r = 1 + 0j$, as verified in Refs. [48,50]. This waveguide-extraction method is preferred over free-space measurements, as it eliminates the plane-wave approximation and diffraction effects and ensures mode and/or energy confinement. It also offers wide bandwidth, high signal strength, and easy sample preparation.

We characterize a number of 3D-printed samples shown in Table I and compare them to accepted literature values to ensure the accuracy of the test setup. We print 10-mm-thick samples of each (100% infill density), using the two most common 3D-printing techniques, fused-deposition modeling (FDM) and polyjet printing. Thermoplastics, including polylactic acid (PLA) [50], polycarbonate [51,52], and acrylonitrile butadiene styrene (ABS) [53] samples are generally fabricated using FDM, while Veroclear [54,55] (a curable photopolymer) is printed on high-resolution polyjet printers that use ultraviolet (UV) light curing to print thin layers until the device is fully formed. The UV curing during polyjet printing is responsible for the high losses in Veroclear. Conversely, PLA is an excellent candidate for the fabrication of our devices, because it has a low loss tangent and a reasonably high permittivity that can support the large range of desired polarizabilities. Furthermore, unlike ABS, it does not show thermal shrinking and warping during printing.

TABLE I. The experimentally extracted permittivity and loss-tangent values of 3D-printed samples.

Material	Re(ϵ_r)	$\tan\delta$
ABS	2.40	0.008
PLA	2.70	0.005
Polycarbonate	2.56	0.010
Veroclear	2.80	0.020

IV. ELEMENT DESIGN AND POLARIZABILITY EXTRACTION

Here, we discuss the design and polarizability extraction of the elements that constitute the devices. For our designs, we use PLA cylinders as building blocks; conveniently, the scattered electric field outside the cylinder is invariant along its axis (the z axis). The field invariance along the z axis allows us to limit our investigation to two dimensions and test the devices in a parallel-plate waveguide with a 11-mm gap between the plates. For successful implementation, as discussed in Sec. A, the cylindrical elements are modeled as being 10 mm tall. Depending on the size of the device, it is composed of hundreds to thousands of cylinders of varying radii, arranged in a square lattice. To connect them all in a single structure, we include a 0.25-mm-thick base layer, as shown in Fig. 3. The thickness of the layer is chosen such that it has negligible scattering and does not affect the mode profile in the parallel-plate waveguide.

We extract the intrinsic polarizability of the cylinders by simulating their scattering in the parallel-plate waveguide

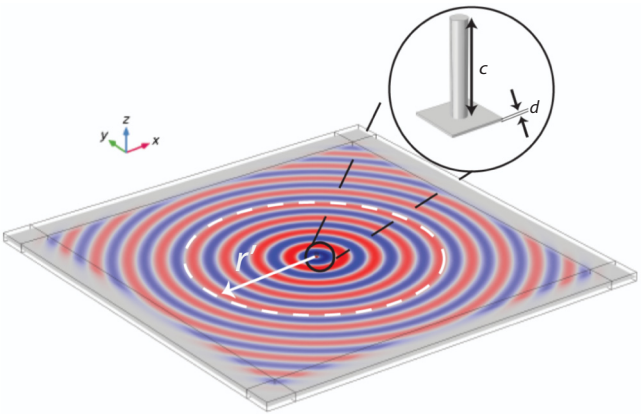

FIG. 3. The electric field scattered in a parallel-plate waveguide by a PLA cylindrical element (inset) placed at its center. The cylinder dimensions are $c = 9.75$ mm and $d = 0.25$ mm; the waveguide height is 11 mm. To extract the element's polarizability, the scattered electric field is integrated over the circle of radius $r' = 120$ mm.

with the commercial full-wave simulation software COMSOL MULTIPHYSICS. We extract the values at the working frequency 10 GHz ($\lambda = 3$ cm). The extraction provides the available range of polarizability (which depends on the geometric constraints on the cylinder, discussed in Sec. V) for device design and fabrication. We use COMSOL's 3D scattering formulation, which lets us simulate the field scattered by a cylinder in the waveguide excited with a TEM plane wave. The cylinder is placed at the center of a lossless waveguide modeled as a 11-mm-tall bounding box, shown in Fig. 3. We apply perfectly matched layer (PML) boundary conditions in the x-y plane to avoid any reflection of electromagnetic waves back in the computational domain and perfect electric conductor (PEC) boundary conditions in the z direction. Since the problem is z invariant, we limit our analysis to the electric field in the z direction.

Analytically, the scattered electric field can be expressed as the superposition of the cylindrical harmonics

$$E_{\rm sc}(r,\phi) = -E_0 \sum_{n=-\infty}^{\infty} b_n j^n H_n^{(2)}(kr)\, e^{-jn\phi}, \tag{4}$$

where E_0 is amplitude of the incident field at the center of the element, n is the mode number, $H_n^{(2)}$ is the nth-order Hankel function of the second kind, and b_n is the scattering coefficient, which can be calculated as [56]

$$b_n = \frac{J_n(mkR)\,J_n'(kR) - mJ_n'(mkR)\,J_n(kR)}{J_n(mkR)\,H_n^{(2)'}(kR) - mJ_n'(mkR)\,H_n^{(2)}(mkR)}. \tag{5}$$

Here, m is the refractive index and R is the radius of the cylinder, J_n is the Bessel function of the first kind, and the prime sign indicates derivation with respect to the radial coordinate.

For subwavelength cylinders ($mkR \ll 1$), the lowest-order mode ($n = 0$) is dominant and the contribution of higher modes may be disregarded:

$$E_{\rm sc}(r) \simeq -b_0 E_0 H_0^{(2)}(kr). \tag{6}$$

To extract the intrinsic polarizability in COMSOL, we first calculate the scattering coefficient by integrating the scattered electric field $E_{\rm sc}$ over a circle of radius $r' = 4\lambda$ with the origin at the center of the cylinder:

$$b_0 = -\frac{1}{2\pi E_0 H_0^{(2)}(kr')}\int_0^{2\pi} E_{\rm sc}(r',\phi)d\phi. \tag{7}$$

The radius r' is chosen large enough such that the higher-order modes have decayed. Theoretically, it can be any large distance away from the cylinder. However, increasing the radius will also increase the size of the computational domain, thus increasing the computational time. We use $r' = 4\lambda$ ($\lambda = 3$ cm), which is sufficient to ensure accurate results and minimum computational time. Then, we calculate the intrinsic polarizability [57,58]

$$\alpha^0 = -\frac{4j\epsilon_0}{k^2}\left(\frac{b_0}{1-b_0}\right). \tag{8}$$

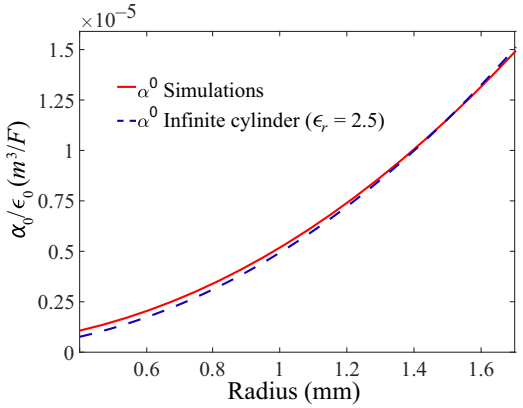

FIG. 4. The intrinsic electric polarizability of the cylinders shown in Fig. 3 (red curve) and of infinite cylinders with $\epsilon_r = 2.5$ (dashed blue curve) at 10 GHz.

To build a library of building blocks, the polarizabilities are extracted using Eq. (8) for a variety of cylinder radii. In the simulations, the cylinder is not infinite, due to the presence of the 1-mm air gap and the base layer in the design. The extracted polarizabilities, however, are close to those of the equivalently sized infinite cylinders, with $\epsilon_r = 2.5$, as shown in Fig. 4 (blue dashed curve). As we show in the next section, we can use these values to simulate cylinders and devices in a 2D full-wave model, thus avoiding the computational burden of 3D simulations.

V. DESIGN CONSTRAINTS

Our design methodology relies on the ability to characterize the scattering elements as equivalent point "dipoles." In a waveguide, a deeply subwavelength cylinder scatters like an infinite line source or, equivalently, as a set of dipoles stacked vertically. As the electrical size of the cylinder increases, however, the energy in the higher-order modes increases and can invalidate our model (which assumes only the lowest-order mode matters), leading to inaccurate designs. In this section, we derive operational bounds for the radius of the constituent PLA cylinders and their lattice spacing, under which the elements are well described as electric line sources. Since the fields are effectively invariant in the vertical direction, we examine the cylinders in 2D and treat them as point "dipoles." Here, we use the term "dipole" improperly, as our examples are in two dimensions, in analogy with the more common 3D formulation of the coupled-dipole model.

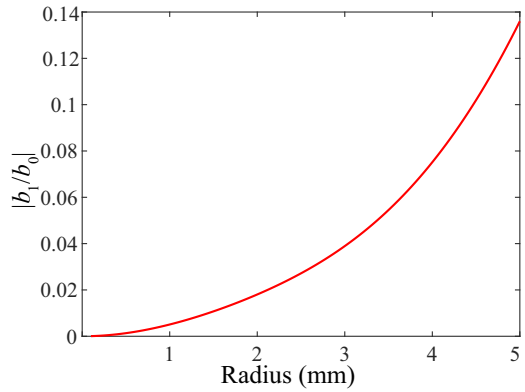

FIG. 5. The ratio of the first-order modes to the lowest-order mode scattering coefficients demonstrates how the higher-order-mode contribution increases with the electrical size of the cylinder.

The lowest- and first-order-mode contributions for a PLA cylinder are assessed by calculating the respective scattering coefficients analytically at 10 GHz using Eq. (5). The higher-order mode ($n = 1$) becomes more significant with respect to the lower mode ($n = 0$) with the increase in cylinder radius. In Fig. 5, the ratio of the quadrupole mode to the lowest-order mode increases quadratically with the cylinder radius. In a lattice, the interference of these higher-order modes degrades the functionality of the device, which is designed with the assumption that $b_n/b_0 \to 0$, for all $n > 0$. Thus, it is important to cap the maximum size of the cylinders. Our analysis has led us to choose the upper limit $R_{\max} = 1.7$ mm, where the plot is linear and the quadrupole contribution is less than 2%. Theoretically, there is no restriction on the minimum size of the cylinder. The resolution of the FDM 3D printers available to us, however, limits cylinders to a minimum radius of $R_{\min} = 0.4$ mm. An additional factor that influences the element interaction is the spacing of the elements. We choose the lattice parameter $a = \lambda/7$. Our choice of maximum and minimum radii and of the lattice parameter provides a good range of polarizability and ensures that the point-dipole model describes the scattering in the fabricated device well.

To calculate the error due to higher-order modes from our choice of maximum cylinder radius and lattice spacing, we simulate two cylinders of $R = R_{\max} = 1.7$ mm kept $\lambda/7$ apart using the coupled-dipole formalism and COMSOL 2D simulations. The electric-field vector is out of plane. While COMSOL simulates all the electromagnetic modes, the coupled-dipole method (CDM) only gives dipolar fields, as shown in Fig. 6. By subtracting the two field plots, we calculate the error introduced by higher-order modes. The magnitude of the error is 2% and is limited to the quasisingular location of each dipole. We show in the results section that this discrepancy does not cause any significant difference between the predicted behavior and the actual behavior of the fabricated devices.

VI. DEVICE FABRICATION

In this section, we discuss the design and fabrication process of simplex (monofunctional) and multiplex (multifunctional) devices at 10 GHz ($\lambda = 3$ cm). For the device functions described in Sec. VI, the symphotic design method provides a set of desired polarizable scatterers in the form of polarizability values. We map these polarizabilities to respective cylinder radii using the data in Fig. 4 (red curve). This gives us a 2D specification of the cylinders and their location in the device. Using the cylinder radii and location data, we create 2D DXF files in MATLAB for the COMSOL simulations.

A computer-aided design (CAD) drawing of the design is constructed in SOLIDWORKS®, a computer-aided design and engineering program. Cylinders are drawn with a

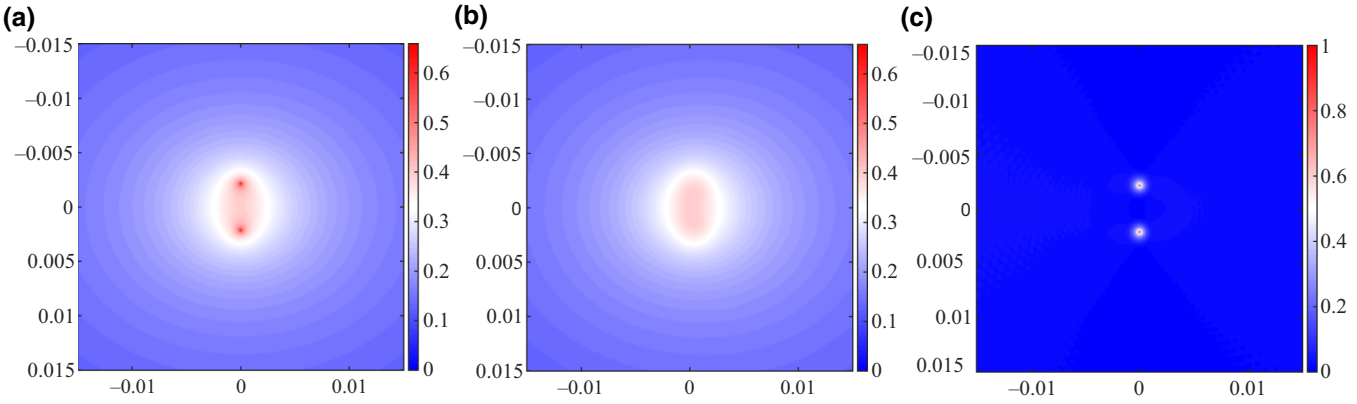

FIG. 6. The magnitudes of the scattered fields E_{sc} for two cylinders of radius $R_{\max} = 1.7$ mm placed $\lambda/7$ apart at 10 GHz. (a) The analytical solution up to the lowest-order mode term. (b) The full-wave simulations in COMSOL MULTIPHYSICS. (c) The relative error, with respect to the analytical solution, $|E_{\text{sc,CDM}}|$.

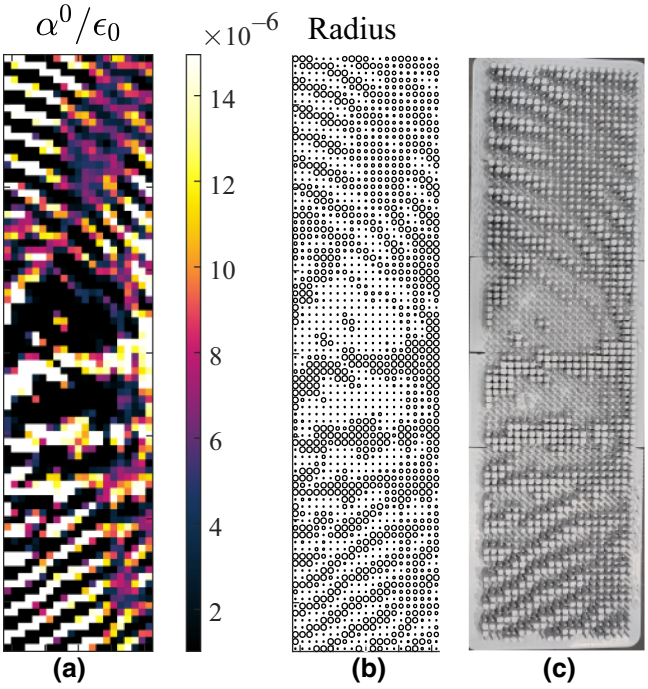

FIG. 7. The design of the 3λ × 12λ simplex device. (a) The intrinsic electric polarizability map. (b) The 2D radius map, showing the relative sizes and positions of cylinders in the device. (c) The 3D-printed PLA device.

height of 10 mm, including a base layer of 0.25 mm. The DXF file type is converted to a 3D STL file (the standard input file type for most 3D printers). The devices

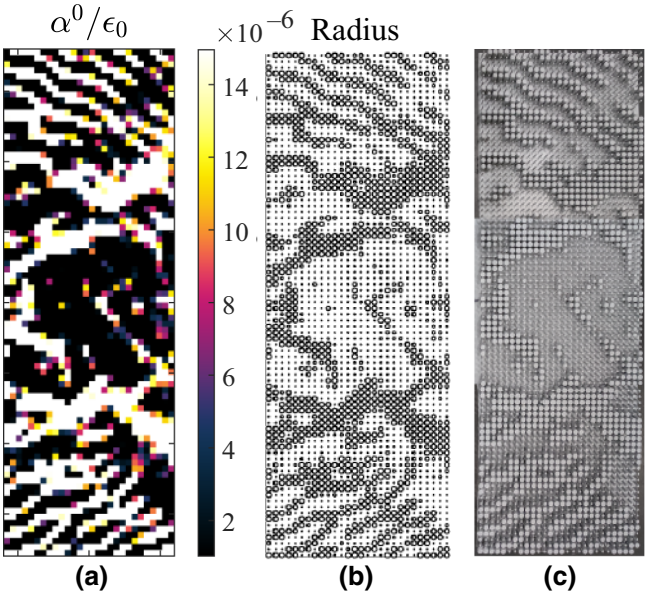

FIG. 8. The design of the 4λ × 12λ multiplex device. (a) The intrinsic electric polarizability map. (b) The 2D radius map, showing the relative radii and positions of cylinders in the device. (c) The 3D-printed PLA device.

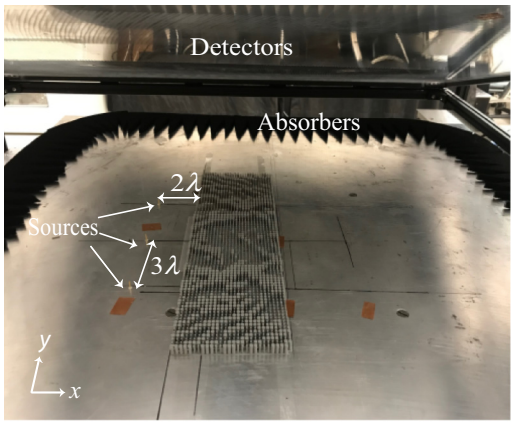

FIG. 9. A photograph of the multiplex device placed inside the 2D field-mapping parallel-plate waveguide.

are printed on an Ultimaker® 3 printer; the STL file is uploaded to the 3D-printer control software and sliced. Slicing converts the STL file to *G* code, which dictates the path followed by the 3D printer for printing. The printing parameters in the 3D slicers are chosen to achieve 100% infill density. Depending on the printer nozzle diameter and temperature, it is possible for the smaller cylinders to be larger than designed due to overextrusion of the filament. The layer height, width, and wall thickness are set

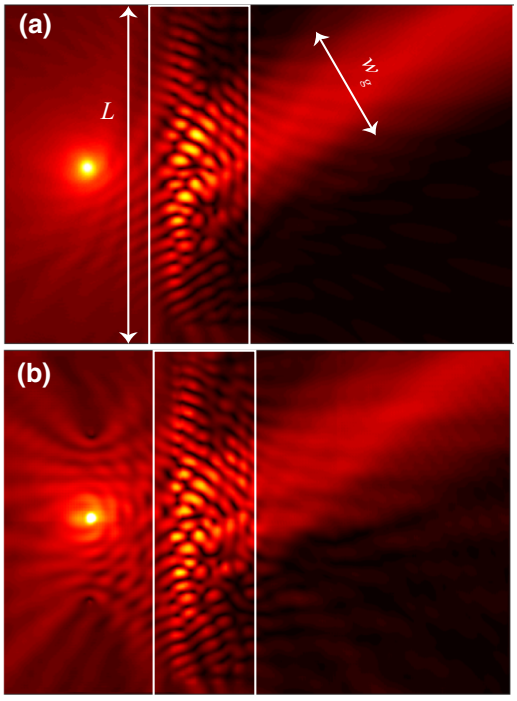

FIG. 10. The simplex device: electric field intensity plots at 10 GHz generated (a) numerically in COMSOL and (b) experimentally in the 2D field mapper. Here, $L = 36$ cm is the length of the device and $w_g = 21$ cm is the beam width.

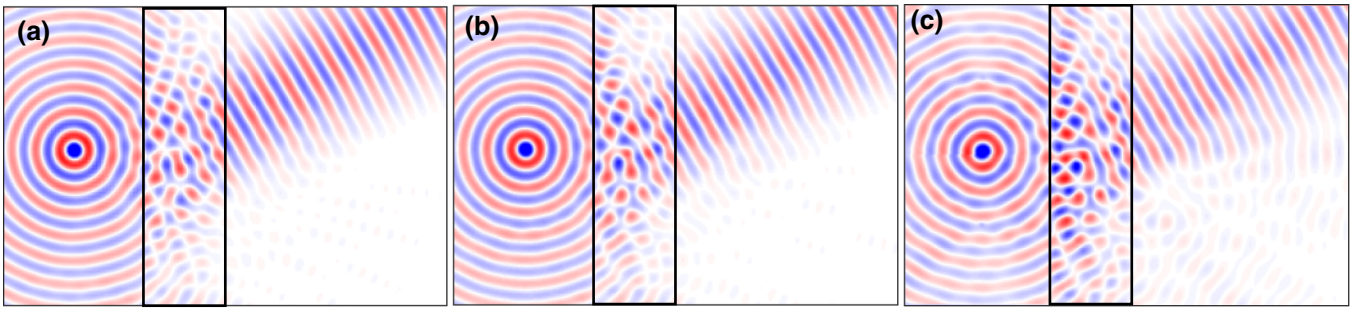

FIG. 11. The simplex device, placed 3λ away from the line source, transforms the incoming line-source field into a Gaussian beam at 30°. The figures show the real part of the electric field at 10 GHz. (a) The analytical solution. (b) Numerical simulation of the device. (c) The experimentally measured spatial field map.

appropriately to minimize dimensional inaccuracies. The size of the devices (chosen to optimize the available field of view of the 2D field mapper where they are characterized) is ultimately larger than the maximum size of the print bed. As such, when necessary, the CAD design is split into multiple prints, which are then reassembled for the experiments.

A simplex device is designed to output a Gaussian beam at 30° when placed 3λ away from a line source centered on the input edge (long side), as shown in Fig. 11(a). The diverging field from the line source is transformed into a Gaussian beam with 94.69% design optimality. The device size is 3λ × 12λ. Figures 7(a) and 7(b) show the polarizability and 2D radii map of the device, respectively. A photograph of the fabricated device is shown in Fig. 7(c).

To demonstrate multiplexing, we assign three functions to our second device shown in Fig. 8 at the same frequency (10 GHz) and polarization, as shown in Figs. 13(a), 13(d), and 13(g). A line source is 2λ away from the input edge of a 4λ × 12λ device. Outgoing Gaussian beams at $\{-30°, -10°, 35°\}$ angles are generated when the source is moved $\{3\lambda, 0, -3\lambda\}$ in the vertical direction, as shown in Fig. 13. The theoretical design optimalities determined for the three functionalities are 89.85%, 93.12%, and 92.67%, respectively.

VII. EXPERIMENTAL RESULTS

A. 2D parallel-plate field mapper

We perform the experiments in a 2D *X*-band field mapper, which is a parallel-plate waveguide [52,59], as shown

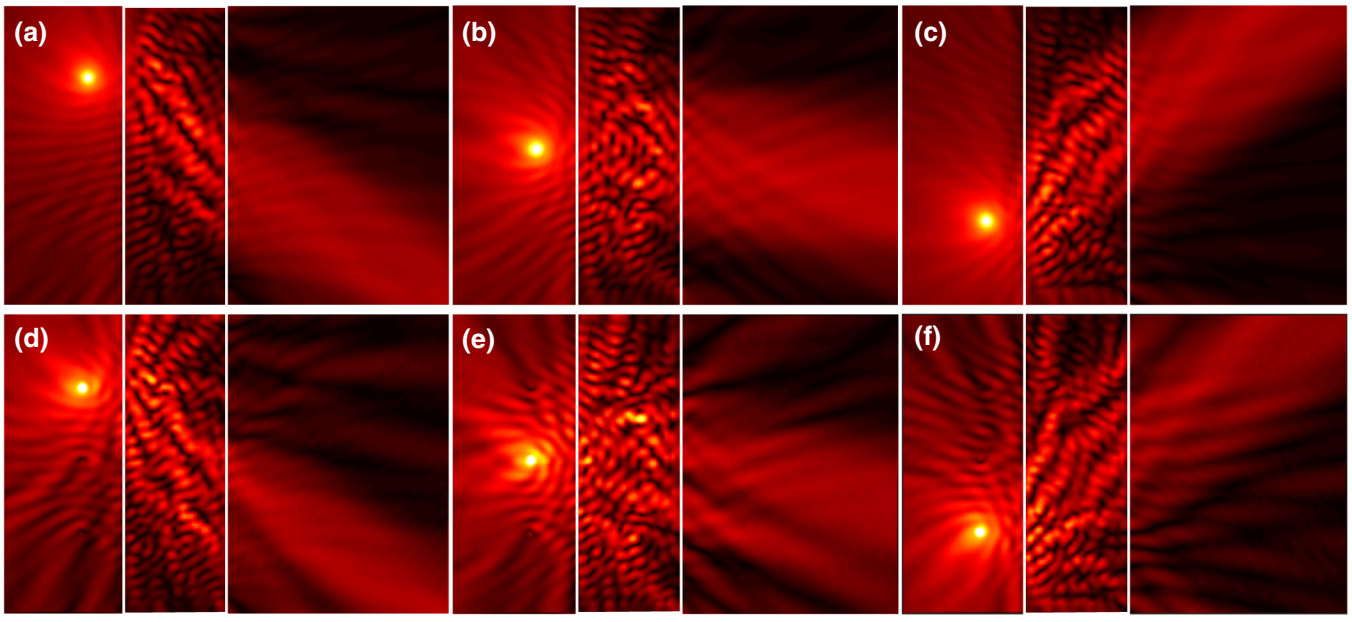

FIG. 12. The multiplex device: electric field intensity plots at 10 GHz generated (a)–(c) numerically in COMSOL and (d)–(f) experimentally in the 2D field mapper.

in Fig. 9. It consists of two aluminum plates separated by a gap of $h = 11$ mm. The VNA feeds the signal to the source and detects the scattering parameter data (S_{21}), which are stored as complex values in matrices and plotted as field maps in MATLAB. A coaxial probe on the lower plate excites a radial wave within the chamber. Since $h < \pi/k$, only the lowest (TEM) mode propagates in the waveguide and the scattering is confined to two dimensions, resulting in field invariance in the direction perpendicular to the plates. Furthermore, the field mapper lets us probe the fields both around and in the interior of the tested device.

The upper waveguide plate (120 cm × 120 cm × 0.63 cm) is equipped with six fixed detection antennas, the measurements of which can be stitched together to measure a large region. The lower waveguide plate (90 cm × 90 cm × 0.63 cm), attached to the optical stages, moves relative to the upper plate while the probe antennas detect the field pattern just below the upper plate. The SIGMA KOKI®, orthogonal X-Y stages (with 100-μm resolution) are controlled by the computer. We fabricate our devices to be 10 mm tall, which leaves a 1-mm air gap between the top of the cylinders and the upper plate. This ensures smooth relative motion between the upper plate and the lower plate supporting the device. Aluminum bars and a structural frame hold the upper plate firmly to avoid sagging (any sag in the upper plate results in undesired artifacts in the field maps). To avoid reflection from the waveguide edges, 10-cm-thick absorbers with a 6-dB/cm attenuation rate are cut in a sawtooth pattern and arranged along the edges of the lower plate. For both experiments, we drill access holes to insert three coaxial ports at different locations into the lower plate. Depending on the desired excitation, the switch activates the appropriate probe, while the others remain inactive and provide minimal undesired scattering.

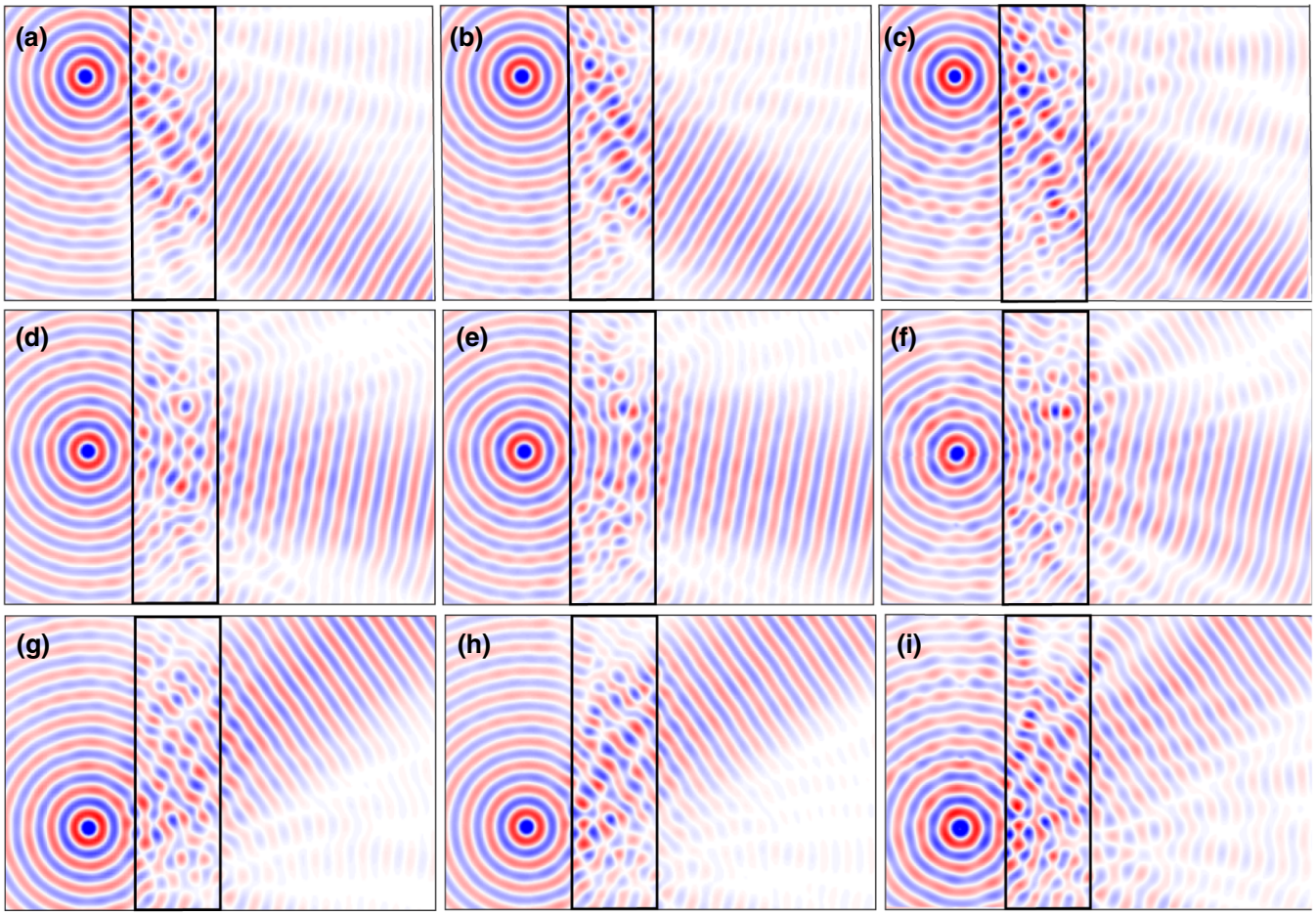

FIG. 13. The multiplex device, placed 2λ away from the line sources, transforms the incoming line-source fields to Gaussian beams at $\{-30^\circ, -10^\circ, 35^\circ\}$ when the source position is shifted by 3λ from top to bottom, respectively. The figures show the real part of the electric field at 10 GHz: (a),(d), (g) the analytical solution; (b),(e), (h) numerical simulation of the device; (c),(f),(i) experimentally measured fields.

TABLE II. For the simplex and multiplex devices, a comparison of the theoretical, simulated (with and without losses), and experimental efficiencies is shown.

Device	Efficiency (%)					Outgoing beam angle (degrees)	
	CDM (lossless)	COMSOL (lossless)	COMSOL (lossy)	Experiment (near field)	Experiment (far field)	CDM	Experiment (far field)
Simplex	71.35	67.94	57.60	56.84	55.93	+30	+32
Multiplex (function 1)	51.14	51.11	42.98	37.86	35.70	−30	−31
Multiplex (function 2)	56.72	52.40	44.30	38.88	34.43	−10	−11
Multiplex (function 3)	59.19	55.85	46.33	36.82	34.41	+35	+37

B. Device measurements

For the simplex-device experiment, we place the printed sample 3λ to the right of the coaxial feed, in agreement with the simulation setup. Despite the scattering due to the two inactive coaxial pins and the dimensional inaccuracies in the device, there is excellent agreement between the analytical, numerical, and experimental results, as shown in Figs. 10 and 11.

For the experimental demonstration of the multiplex device, we introduce three coaxial feeds 3λ apart from each other in the mapper, as shown in Fig. 9. Figure 13 shows the field maps of each functionality. The VNA records measurements for each port individually when it is active. There is a small amount of scattering due to the inactive coaxial pins in the field maps. The device shows excellent agreement with both the coupled-dipole and COMSOL simulations Figs. 12 and 13, despite the slightly perturbed line-source incident fields.

The device efficiency and outgoing beam angles are calculated for theoretical, simulated, and fabricated devices. Here, we define the device efficiency as the ratio of the output Gaussian beam power to the input power. For the input power, a line integral is performed along what would be the left interface of the device in a simulated or experimental field map without the device. This ensures we capture the total power that is incident on the interface from the feed. The output power going into the Gaussian beam is calculated by integrating along a line perpendicular to the direction of the beam. Table II shows the calculated values using

$$\eta_d = \frac{\int^{w_g} |E_{\text{out}}|^2 \, dl}{\int^{L} |E_{\text{in}}|^2 \, dl}, \tag{9}$$

where L is the length of the device and w_g is the width of the beam. The experimental near-field efficiency is calculated from the electric field values collected during the scans, while the obtained fields are propagated to the far field to calculate the far-field efficiency using the aforementioned method.

We note that we get excellent consistency between the simulations and experiments once material losses are included in the COMSOL full-wave simulation. The remaining small discrepancy is likely due to losses associated with the experimental setup. Further, the direction of the predicted and realized beams are in very close agreement.

VIII. CONCLUSION

We present a comprehensive design and fabrication method for the engineering of multifunctional electromagnetic devices using the symphotic method. We use this method to demonstrate all-dielectric high-efficiency simplex and multiplex devices, the operation of which shows excellent agreement between the coupled-dipole model, the full-wave simulations, and the experiment. Each step is repeatable and we can easily fabricate multiplexing devices for any desired input-output waveform. This approach provides a viable path to realizing real-world devices and is robust to manufacturing variation and perturbation of the incident fields. It is a promising candidate for applications that require multiple input-output operations. At microwave frequencies, routing and beam-steering applications can benefit from a simple passive device that offers high efficiency and low crosstalk. At optical frequencies, these techniques can be adopted to enable a host of optical communication and sensing devices, such as interconnects for optical circuits and physical-layer analog optical operators for optical computing. Furthermore, the ability to encode multiple fields (information) in a single volume can address the rapidly growing demand for high-density storage media and help revive the field of optical "holographic" memory.

Finally, we note that the symphotic design method is used here to build devices that multiplex at a single frequency. We suggest that its utility can be extended to develop devices multiplexing over some bandwidth. This could advance multispectral imaging and sensing applications and boost optical transmission systems by encoding multiple signals at different wavelengths. The simultaneous encoding of multiple transformations would increase data access and optical computing speeds.

ACKNOWLEDGMENTS

This work was supported by the Air Force Office of Scientific Research under Contract No. FA95501810187. We

would also like to acknowledge the support of the Innovation CO-LAB at Duke University, where the devices were fabricated. Finally, we would like to thank Patrick Bowen and Mohammadreza F. Imani for helpful discussions.

[1] Rafael Piestun and Joseph Shamir, Control of wave-front propagation with diffractive elements, Opt. Lett. **19**, 771 (1994).
[2] Rafael Piestun, Boris Spektor, and Joseph Shamir, Wave fields in three dimensions: Analysis and synthesis, J. Opt. Soc. Am. A **13**, 1837 (1996).
[3] Rafael Piestun and Joseph Shamir, Synthesis of three-dimensional light fields and applications, Proc. IEEE **90**, 222 (2002).
[4] Wenjian Cai, Ariel R. Libertun, and Rafael Piestun, Polarization selective computer-generated holograms realized in glass by femtosecond laser induced nanogratings, Opt. Express **14**, 3785 (2006).
[5] Tim D. Gerke and Rafael Piestun, Aperiodic computer-generated volume holograms improve the performance of amplitude volume gratings, Opt. Express **15**, 14954 (2007).
[6] Tim D. Gerke and Rafael Piestun, Aperiodic volume optics, Nat. Photonics **4**, 188 (2010).
[7] Rafael Piestun and David A. B. Miller, Electromagnetic degrees of freedom of an optical system, J. Opt. Soc. Am. **17**, 892 (2000).
[8] Rafael Piestun and C. Martijn de Sterke, Fundamental limit for two-dimensional passive devices, Opt. Lett. **34**, 779 (2009).
[9] Jesse Lu, Stephen Boyd, and Jelena Vučković, Inverse design of a three-dimensional nanophotonic resonator, Opt. Express **19**, 10563 (2011).
[10] Jesse Lu, Jelena Vučković, Nanophotonic computational design, Opt. Express **21**, 13351 (2013).
[11] Alexander Y. Piggott, Jesse Lu, Thomas M. Babinec, Konstantinos G. Lagoudakis, Jan Petykiewicz, and Jelena Vučković, Inverse design and implementation of a wavelength demultiplexing grating coupler, Sci. Rep. **4**, 7210 (2014).
[12] Alexander Y. Piggott, Jesse Lu, Konstantinos G. Lagoudakis, Jan Petykiewicz, Thomas M. Babinec, and Jelena Vučković, Inverse design and demonstration of a compact and broadband on-chip wavelength demultiplexer, Nat. Photonics **9**, 374 (2015).
[13] Alexander Y. Piggott, Jan Petykiewicz, Logan Su, and Jelena Vučković, Fabrication-constrained nanophotonic inverse design, Sci. Rep. **7**, 1786 (2017).
[14] Logan Su, Alexander Piggott, Neil V. Sapra, Jan Petykiewicz, and Jelena Vuckovic, Inverse design and demonstration of a compact on-chip narrowband three-channel wavelength demultiplexer, ACS Photon. **5**, 301 (2018).
[15] Logan Su, Rahul Trivedi, Neil V. Sapra, Alexander Y. Piggott, Dries Vercruysse, and Jelena Vučković, Fully-automated optimization of grating couplers, arXiv:1711.02228 (2017).
[16] Christopher M. Lalau-Keraly, Samarth Bhargava, Owen D. Miller, and Eli Yablonovitch, Adjoint shape optimization applied to electromagnetic design, Opt. Express **21**, 21693 (2013).
[17] Vidya Ganapati, Owen D. Miller, and Eli Yablonovitch, Light trapping textures designed by electromagnetic optimization for subwavelength thick solar cells, IEEE J. Photovolt. **4**, 175 (2013).
[18] Chia Wei Hsu, Owen D. Miller, Steven G. Johnson, and Marin Soljačić, Optimization of sharp and viewing-angle-independent structural color, Opt. Express **23**, 9516 (2015).
[19] Roberto Zecca, Daniel L. Marks, and David R. Smith, Variational design method for dipole-based volumetric artificial media, Opt. Express **27**, 6512 (2019).
[20] Edward M. Purcell and Carlton R. Pennypacker, Scattering and absorption of light by nonspherical dielectric grains, Astrophys. J. **186**, 705 (1973).
[21] Bruce T. Draine, The discrete-dipole approximation and its application to interstellar graphite grains, Astrophys. J. **333**, 848 (1988).
[22] John J. Goodman, Piotr J. Flatau, and Bruce T. Draine, Application of fast-Fourier-transform techniques to the discrete-dipole approximation, Opt. Lett. **16**, 1198 (1991).
[23] Akhlesh Lakhtakia, General theory of the Purcell-Pennypacker scattering approach and its extension to bianisotropic scatterers, Astrophys. J. **394**, 494 (1992).
[24] Bruce T. Draine and Piotr J. Flatau, Discrete-dipole approximation for scattering calculations, J. Opt. Soc. Am. A **11**, 1491 (1994).
[25] David R Smith, Willie J. Padilla, D. C. Vier, Syrus C. Nemat-Nasser, and Seldon Schultz, Composite Medium with Simultaneously Negative Permeability and Permittivity, Phys. Rev. Lett. **84**, 4184 (2000).
[26] Maxim A. Yurkin and Alfons G. Hoekstra, The discrete dipole approximation: An overview and recent developments, J. Quant. Spectrosc. Radiat. Transfer **106**, 558 (2007).
[27] F. Magnus, B. Wood, J. Moore, Kelly Morrison, G. Perkins, J. Fyson, M. C. K. Wiltshire, D. Caplin, L. F. Cohen, and J. B. Pendry, A dc magnetic metamaterial, Nat. Mater. **7**, 295 (2008).
[28] Joerg Petschulat, C. Menzel, A. Chipouline, C. Rockstuhl, A. Tünnermann, F. Lederer, and T. Pertsch, Multipole approach to metamaterials, Phys. Rev. A **78**, 043811 (2008).
[29] Patrick T. Bowen, Tom Driscoll, Nathan B. Kundtz, and David R. Smith, Using a discrete dipole approximation to predict complete scattering of complicated metamaterials, New J. Phys. **14**, 033038 (2012).
[30] Alexander N. Poddubny, Pavel A. Belov, Pavel Ginzburg, Anatoly V. Zayats, and Yuri S. Kivshar, Microscopic model of Purcell enhancement in hyperbolic metamaterials, Phys. Rev. B **86**, 035148 (2012).
[31] Mikala Johnson, Patrick Bowen, Nathan Kundtz, and Adam Bily, Discrete-dipole approximation model for control and optimization of a holographic metamaterial antenna, Appl. Opt. **53**, 5791 (2014).
[32] Laura M. Pulido-Mancera, Tomas Zvolensky, Mohammadreza F. Imani, Patrick T. Bowen, Minu Valayil, and David R. Smith, Discrete dipole approximation applied to

highly directive slotted waveguide antennas, IEEE Antennas Wireless Propag. Lett. **15**, 1823 (2016).
[33] Mohammadreza F. Imani, Timothy Sleasman, Jonah N. Gollub, and David R. Smith, Analytical modeling of printed metasurface cavities for computational imaging, J. Appl. Phys. **120**, 144903 (2016).
[34] A Brioude and M. P. Pileni, Silver nanodisks: Optical properties study using the discrete dipole approximation method, J. Phys. Chem. B **109**, 23371 (2005).
[35] Prashant K. Jain, Susie Eustis, and Mostafa A. El-Sayed, Plasmon coupling in nanorod assemblies: Optical absorption, discrete dipole approximation simulation, and exciton-coupling model, J. Phys. Chem. B **110**, 18243 (2006).
[36] Z.-Y. Zhang and Y.-P. Zhao, Optical properties of helical Ag nanostructures calculated by discrete dipole approximation method, Appl. Phys. Lett. **90**, 221501 (2007).
[37] Vincenzo Amendola, Osman M. Bakr, and Francesco Stellacci, A study of the surface plasmon resonance of silver nanoparticles by the discrete dipole approximation method: Effect of shape, size, structure, and assembly, Plasmonics **5**, 85 (2010).
[38] Roberto Zecca, Daniel L. Marks, and David R. Smith, Symphotic design of an edge detector for autonomous navigation, IEEE Access **7**, 144836 (2019).
[39] Salim Boutami and Shanhui Fan, Efficient pixel-by-pixel optimization of photonic devices utilizing the Dyson's equation in a Green's function formalism: Part I. Implementation with the method of discrete dipole approximation, J. Opt. Soc. Am. B **36**, 2378 (2019).
[40] Salim Boutami and Shanhui Fan, Efficient pixel-by-pixel optimization of photonic devices utilizing the Dyson's equation in a Green's function formalism: Part II. Implementation using standard electromagnetic solvers, J. Opt. Soc. Am. B **36**, 2387 (2019).
[41] Max Born, Quantenmechanik der Stoßvorgänge, Z. Phys. A **38**, 803 (1926).
[42] Daniel L. Marks and David R. Smith, Inverse scattering with a non self-adjoint variational formulation, Opt. Express **26**, 7655 (2018).
[43] Chun Hsiung Chen and Chuen-Der Lien, The variational principle for non-self-adjoint electromagnetic problems, IEEE Trans. Microw. Theory Techn. **28**, 878 (1980).
[44] Douglas Kent Rytting, in *Proc. RF Microw. Meas. Symp. Exhib.* (Citeseer, Santa Rosa, CA, 1991), p. 1.
[45] Andrew Davidson, Eric Strid, and Keith Jones, in *34th ARFTG Conference Digest* (IEEE, Fort Lauderdale, FL, 1989), Vol. 16, p. 61.
[46] Glenn F. Engen and Cletus A. Hoer, Thru-reflect-line: An improved technique for calibrating the dual six-port automatic network analyzer, IEEE Trans. Microw. Theory Tech. **27**, 987 (1979).
[47] Hewlett-Packard Product Note, 8510-8: Applying the HP 8510b TRL calibration for non-coaxial measurements (1987).
[48] William B. Weir, Automatic measurement of complex dielectric constant and permeability at microwave frequencies, Proc. IEEE **62**, 33 (1974).
[49] Thomas Zwick, Arun Chandrasekhar, Christian W. Baks, Ullrich R. Pfeiffer, Steven Brebels, and Brian P. Gaucher, Determination of the complex permittivity of packaging materials at millimeter-wave frequencies, IEEE Trans. Microw. Theory Tech. **54**, 1001 (2006).
[50] João M. Felício, Carlos A. Fernandes, and Jorge R. Costa, in *2016 22nd International Conference on Applied Electromagnetics and Communications (ICECOM)* (IEEE, Dubrovnik, Croatia, 2016), p. 1.
[51] Rene Grignon, Mohammed N. Afsar, Yong Wang, and Saquib Butt, in *Proceedings of the 20th IEEE Instrumentation Technology Conference (Cat. No. 03CH37412)* (IEEE, Vail, Colorado, 2003), Vol. 1, p. 865.
[52] Bryan J. Justice, Jack J. Mock, Liheng Guo, Aloyse Degiron, David Schurig, and David R. Smith, Spatial mapping of the internal and external electromagnetic fields of negative index metamaterials, Opt. Express **14**, 8694 (2006).
[53] Yaroslav Urzhumov, Nathan Landy, Tom Driscoll, Dimitri Basov, and David R. Smith, Thin low-loss dielectric coatings for free-space cloaking, Opt. Lett. **38**, 1606 (2013).
[54] Jianjia Yi, Gérard-Pascal Piau, André De Lustrac, and Shah Nawaz Burokur, Electromagnetic field tapering using all-dielectric gradient index materials, Sci. Rep. **6**, 30661 (2016).
[55] Sence Johann, Feuray William, Périgaud Aurélien, Tantot Olivier, Delhote Nicolas, Stéphane Bila, Verdeyme Serge, Pejoine Jean-Baptiste, and René-Philippe Gramond, in *2016 46th European Microwave Conference (EuMC)* (IEEE, London, UK, 2016), p. 373.
[56] Craig F. Bohren and Donald R. Huffman, *Absorption and Scattering of Light by Small Particles* (John Wiley & Sons, New York, 2008).
[57] Patrick T. Bowen, Ph.D. thesis, Duke University, 2017.
[58] Laura Pulido-Mancera, Patrick T. Bowen, Mohammadreza F. Imani, Nathan Kundtz, and David Smith, Polarizability extraction of complementary metamaterial elements in waveguides for aperture modeling, Phys. Rev. B **96**, 235402 (2017).
[59] John Hunt, Gyushik Jang, and David R. Smith, Perfect relay lens at microwave frequencies based on flattening a Maxwell lens, J. Opt. Soc. Am. **28**, 2025 (2011).